

Monitoring Observations of SMC X-1’s Excursions (MOOSE) III: X-ray Spectroscopy of a Warped, Precessing Accretion Disc

Rawan Karam,^{1,2,3}★ Kristen C. Dage^{2,3,4,7} †, Bailey E. Tetarenko,^{2,3} McKinley C. Brumback^{5,6}, Daryl Haggard^{2,3} Arash Bahramian,⁷ Chin-Ping Hu,⁸ Joey Neilsen,⁹ Diego Altamirano,¹⁰ Wasundara Athukoralalage,^{11,12} Philip A. Charles,¹⁰ William I. Clarkson,¹³ Ryan C. Hickox,¹⁴ Jamie Kennea¹⁵

¹ *Département de Physique, Université de Montréal, Succ. Centre-Ville, Montréal, Québec, H3C 3J7, Canada*

² *Department of Physics, McGill University, 3600 University Street, Montréal, QC H3A 2T8, Canada*

³ *Trottier Space Institute at McGill 3550 University Street, Montréal, QC H3A 2A7, Canada*

⁴ *Wayne State University, Department of Physics & Astronomy, 666 W Hancock St, Detroit, MI 48201, USA*

⁵ *Department of Physics, Middlebury College, Middlebury, VT 05753, USA*

⁶ *Department of Astronomy, University of Michigan, 1085 S. University Ave. Ann Arbor, MI 48109 USA*

⁷ *International Centre for Radio Astronomy Research – Curtin University, GPO Box U1987, Perth, WA 6845, Australia*

⁸ *Department of Physics, National Changhua University of Education, Changhua, 50007, Taiwan*

⁹ *Villanova University, Department of Physics, Villanova, PA 19085, USA*

¹⁰ *Physics & Astronomy, University of Southampton, Southampton, Hampshire SO17 1BJ, UK*

¹¹ *Center for Astrophysics | Harvard & Smithsonian, 60 Garden Street, Cambridge, MA 02138-1516, USA*

¹² *Department of Physics and Astronomy, Michigan State University, East Lansing, MI 48824, USA*

¹³ *Department of Natural Sciences, University of Michigan-Dearborn, 4901 Evergreen Rd. Dearborn, MI 48128, USA*

¹⁴ *Department of Physics & Astronomy, Dartmouth College, 6127 Wilder Laboratory, Hanover, NH 03755, USA*

¹⁵ *Department of Astronomy and Astrophysics, The Pennsylvania State University, University Park, PA 16802, USA*

Accepted XXX. Received YYY; in original form ZZZ

ABSTRACT

The MOOSE (Monitoring Observations of SMC X-1’s Excursions) program uses the Neutron Star Interior Composition Explorer Mission (NICER) to monitor the high mass X-ray binary SMC X-1 during its superorbital period excursions. Here we perform X-ray spectral analyses of 26 NICER observations of SMC X-1, taken at the tail-end of the excursion between 2021-04-01 and 2022-01-05. We use a single spectral model to fit spectra observed in high, intermediate and low states, using a combination of a partial covering fraction model, a black-body disc, and a power-law component. We find that the partial covering fraction varies significantly with the superorbital state during superorbital excursion. Our findings suggest that the low/high state in SMC X-1 is caused by a very high obscuration of the accretion disk.

Key words: accretion, accretion discs – stars: pulsars: individual: SMC X-1 – X-rays: binaries

1 INTRODUCTION

Warped accretion discs challenge our current models and understanding of accretion physics. Many studies now suggest that warped accretion discs are far more ubiquitous than previously thought, and are present in black holes and neutron star systems alike (Townsend & Charles 2020; Thomas et al. 2022). For example, Clarkson et al. (2003) demonstrated that many systems display superorbital periods (detected periods longer than the binary orbit) with varying lengths, which are due to warped accretion discs, where the stability of the warp is determined by properties of the binary system, such as binary separation and binary mass ratio (Ogilvie & Dubus 2001). Smoothed particle hydrodynamic simulations (e.g. Foulkes et al. 2006) have indicated that the central engine’s illumination of the accretion disc can

exert non-axisymmetric radiation, which causes tilting or warping on the disc’s surface.

The neutron star X-ray binary SMC X-1 is one of the best systems in which to study the physics behind accretion discs due to its well-determined distance, low extinction and variety of time dependent behavior. SMC X-1’s orbital period is 3.89 days with a pulse period of 0.7 seconds (Lucke et al. 1976), and it exhibits a superorbital period of 40–60 days (Wojdowski et al. 1998; Gruber & Rothschild 1984). This is likely due to a warped, precessing accretion disc (Clarkson et al. 2003; Hickox et al. 2004; Brumback et al. 2020). SMC X-1’s superorbital period is nominally ~ 55 days, but is observed to change to as low as 45 days (Figure 1), a so-called superorbital period “excursion”, which occurs when the collimated radiation hits the accretion disc, changing its geometry (Foulkes et al. 2006). The broad-band X-ray spectrum has been characterized as a cut-off power law continuum with a low energy blackbody component and iron emission lines by various instruments and studies including ASCA

★ E-mail: rawan.karam@mail.mcgill.ca

† NASA Einstein Fellow

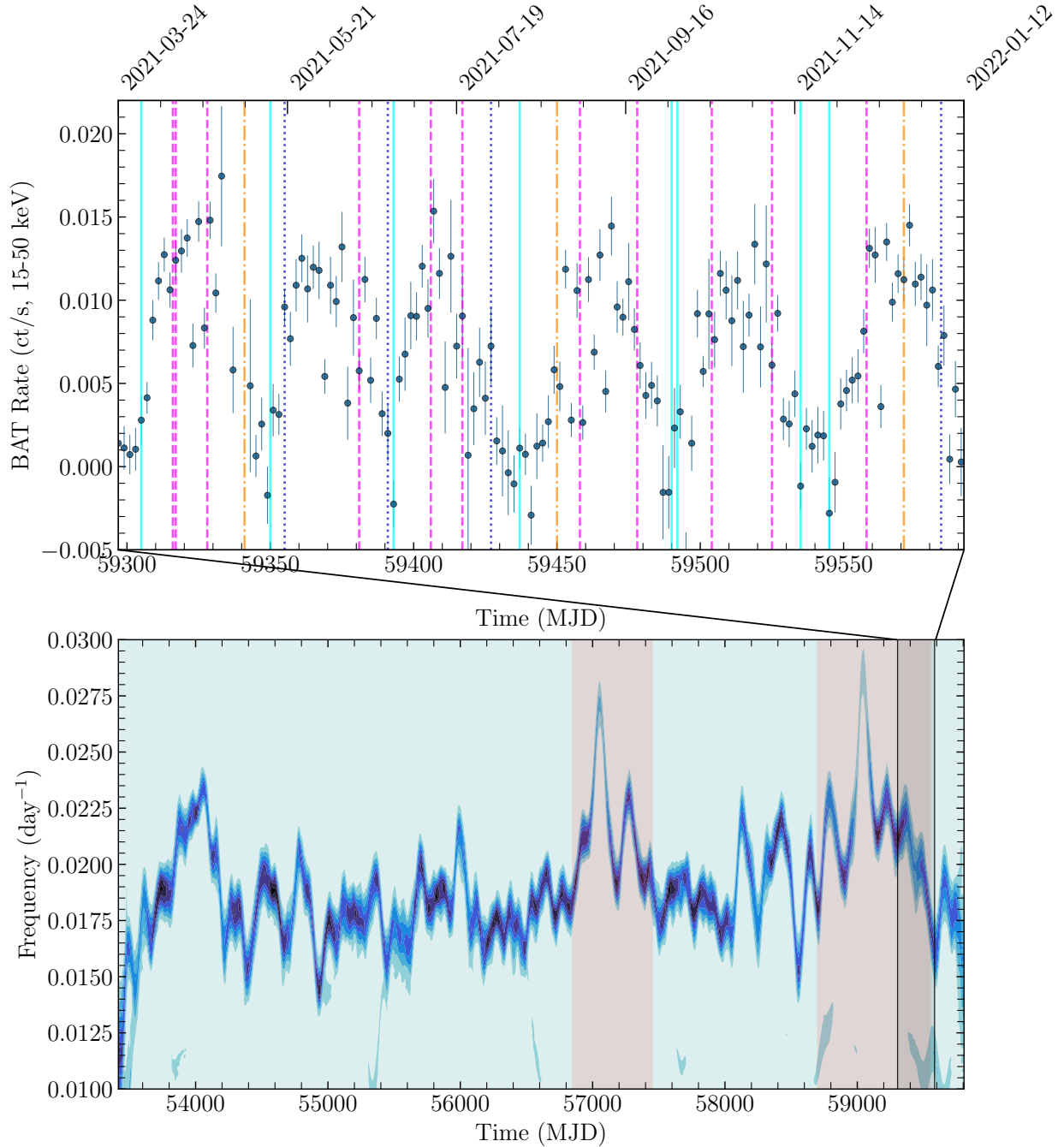


Figure 1. Hilbert-Huang transform of SMC X-1 (from Hu et al. 2023) showing three of its superorbital period excursions. The inset at MJD 59305 shows the *Swift*/BAT lightcurve of SMC X-1 overlaid with observation times from our NICER monitoring campaign (pink dashed are high state observations, blue dotted lines are intermediate state observations, aqua solid lines are low state observations and gold dash-dot lines are pre-eclipse dips), taken during the tail-end of the superorbital period excursion. Our observations span a range of superorbital phases and source luminosity. The grey shaded regions mark the duration of the third and fourth superorbital excursions, respectively. Our observations span the tail end of the fourth excursion and continue after the excursion has finished.

(Paul et al. 2002), Beppo-SAX (Naik & Paul 2004), XMM-Newton and NuSTAR (Brumback et al. 2020), and NICER (Dage et al. 2022).

SMC X-1’s superorbital period has been a long-standing subject of investigation since Gruber & Rothschild (1984), which observed the variability and spectrum of SMC X-1 with observations from the UCSD/MIT instrument on HEAO 1 from 1977 to 1979. Their results suggest that SMC X-1 has two states, high or low, and they constructed average spectra separately for each state, which showed

that the total emission from SMC X-1 displays a continuum spectrum with a dominant exponential form. More recent studies using XMM-Newton and NuSTAR’s combined broad-band X-ray coverage reveal that the superorbital high and low states exhibit different X-ray continua and suggest higher absorption during the low states (Pike et al. 2019; Brumback et al. 2020), consistent with observation from a precessing warped accretion disk. Pradhan et al. (2020) examined archival Suzaku and NuSTAR spectra of SMC X-1 during different

superorbital states and noted large changes in the normalization of the power law component that suggest an additional mechanism may be driving SMC X-1's spectral changes with superorbital phase.

SMC X-1 also exhibits timing behaviors beyond its superorbital period, including an energy dependent pulse profile and binary eclipses. Beppo-SAX observations of SMC X-1 revealed a single peaked pulse profile at energies below 1 keV and a double peaked profile at higher energies (Naik & Paul 2004). These results were confirmed by observations using Chandra, XMM-Newton, and NuSTAR. Hickox & Vrtillek (2005) and Brumback et al. (2020) performed pulse-phase resolved spectroscopy of SMC X-1 and found that the blackbody component of the X-ray spectrum followed the low energy pulse profile and the power-law component followed the high energy power law, similar to ASCA studies by Paul et al. (2002). These studies suggest that the soft component is likely produced by reprocessing of the hard X-ray pulsar beam by the inner accretion disc. They support this claim by using a model of a twisted inner disc illuminated by the rotating X-ray pulsar beam to simulate pulsations in the soft component, thus showing that the precession of an illuminated accretion disc can roughly reproduce the observed long-term changes in the soft-pulse profiles for some disc and beam geometries (Hickox & Vrtillek 2005; Brumback et al. 2020).

Studies of the X-ray orbital light curve of SMC X-1 have revealed it to have pre-eclipse dips in the orbital phase range of 0.6-0.85 (e.g., Woo et al. 1995; Raichur & Paul 2010; Hu et al. 2013a; Brumback et al. 2022). While not well studied, these dips are thought to be similar to those seen in Her X-1 (Giacconi et al. 1973), and are caused by increased obscuration from the impact of the accretion stream onto the accretion disc.

SMC X-1's superorbital excursions offer a rare chance to study both pulsar behaviour and the accretion disc at the same time. Dage et al. (2019) and Hu et al. (2019) highlighted that the superorbital period and the spin of SMC X-1 may be both correlated with the physics behind the accretion. Hu et al. (2013b) applied the Hilbert-Huang transform to analyse the time-frequency properties of the superorbital modulation in SMC X-1 from observations made by the All-Sky Monitor onboard the Rossi X-ray Timing Explorer. The resultant Hilbert spectrum showed that the superorbital modulation period varied between ~ 40 and ~ 60 days, providing a robust timing technique that could very closely follow the changes in the superorbital period.

Later analysis of SMC X-1 by Hu et al. (2019) showed that a third observed superorbital period excursion event occurred during 2014-2016 and suggests that this excursion is recurrent and possibly periodic. Brumback et al. (2020) modeled the geometry of SMC X-1 and showed that superorbital period cycles are indeed consistent with a warped accretion disc. However, a similar analysis has not yet been completed for data taken during a superorbital period excursion, and it is not known whether the geometry of the disc changes as the superorbital period changes. Stray-light studies of SMC X-1 with NuSTAR found that SMC X-1's pulse profile did not vary with energy, but did change significantly over time (Brumback et al. 2022).

A study of SMC X-1 by Pike et al. (2019) suggests that its transient pulsations may be due to obscuration of the warped accretion disc. Thus, understanding the physical processes behind accretion is the first step to addressing the superorbital period, and understanding SMC X-1 may help shed light on the more extreme processes happening in the more distant pulsating ultraluminous X-ray sources, some of which show similar long-term variability (Bachetti et al. 2020; Townsend & Charles 2020).

The first paper in this series, MOOSE I, Dage et al. (2022) introduces the first 26 observations of the MOOSE campaign and provides

spectral fits to the high state spectra of SMC X-1 as it exits its fourth epoch of superorbital period excursion (Figure 1). In these high-state spectral fits, Dage et al. (2022) found very little fluctuation between key spectral parameters like absorption column density, black-body disc temperature, and photon index. MOOSE II (Hu et al. 2023) studies the excursion phenomenon in SMC X-1 specifically, comparing the properties of the most recent excursion event (2020-2021 or MJD 58700-59550, see Figure 1) to prior excursions. Their study of the superorbital period finds that the spin-up acceleration and the pulse profiles (the shape of the pulsations emanating from the neutron star) may be connected to the superorbital excursion. These behaviours suggest that SMC X-1 is a complex physical system that requires more than a simple warped disc model (see also Pradhan et al. 2020).

Dage et al. (2022) studied 11 NICER high-state observations (out of the 26 observations taken during the tail-end of excursion) and found no evidence for significant changes in the spectral shape of the superorbital high state. In this work, we present the first spectral fits to all 26 of the NICER observations to investigate spectral changes between superorbital high, intermediate, and low states and to examine if the spectral shapes change after the end of excursion. We present the data and analysis in Section 2 and discuss the results in Section 3. Our conclusions and recommendations for future work are presented in Section 4.

2 OBSERVATIONS AND DATA ANALYSIS

We analysed 26 observations within the MOOSE data set of SMC X-1, taken with the Neutron Star Interior Composition Explorer (NICER; Gendreau et al. 2016). These observations were taken in random intervals of at least 10 days, spanning different stages of the superorbital cycle (specifically the high, intermediate and low states), from 2021-04-01 (MJD 59305) until 2022-01-05 (MJD 59584). Most observations were taken towards the end of the 2020-2021 superorbital excursion, defined as the time interval from MJD 58700 to 59550 (Hu et al. 2023). The final three observations occurred after this excursion epoch (see Figure 1 and Table 1).

2.1 NICER

The NICER observations were processed with HEASOFT 6.29 NICERL2 task. For each observation, the spectrum was generated with the XSELECT command, with optimal binning implemented (Kaastra & Bleeker 2016). For the background, the spectra were generated with the NIBACKGEN3C50 tool (Remillard et al. 2022). The NICERARF and NICERRMF tasks were used to generate the ancillary response files (ARF) and response matrix files (RMF). This data reduction follows the method used in Dage et al. (2022), where it is described in detail. Further information including date, exposure, count rate, and other filtering parameters can be found in Table 1.

2.2 X-ray Spectral Fitting

Working with these spectra, we tested a series of models to fit the 0.3-12 keV energy range for all observations. We used XSPEC v12.12.0 (Arnaud 1996) to model the spectra, using χ^2 statistics, abundances from Wilms et al. (2000), and photo-electric cross sections from Verner et al. (1996).

We implemented a model with an interstellar medium absorption component (tbabs) and a partial covering component (pcfabs) to assess the degree of obscuration from the warped accretion disc (e.g.,

Table 1. NICER observations log with count rate errors determined by `xspec`. Pre-eclipse dips are marked with †.

ObsID	Date	Duration (s)	Overonly Range	Underonly Range	Count Rate (ct/s)
4509010101	2021-04-01	1006	<11	<200	33 ± 0.2
4509010102	2021-04-12	1362	<3	<200	214 ± 0.4
4509010103	2021-04-13	483	<7	<200	220 ± 0.6
4509010301	2021-04-24	436	<20	<200	195 ± 0.7
4509010401 †	2021-05-07	967	<40	<200	2 ± 0.05
4509010501	2021-05-16	1446	<140	<200	7 ± 0.07
4509010601	2021-05-21	1024	<4	<200	146 ± 0.4
4509010701	2021-06-16	1279	<2	<200	206 ± 0.4
4509010801	2021-06-26	1684	<1.5	<200	139 ± 0.3
4509010802	2021-06-28	796	<20	<200	10 ± 0.2
4509010803	2021-07-11	944	<30	<200	232 ± 0.5
4509010901	2021-07-22	821	<20	<200	179 ± 0.4
4509011001	2021-08-01	1235	<50	<200	72 ± 0.3
4509011101	2021-08-11	1123	<1	<200	9 ± 0.1
4509011201 †	2021-08-24	1327	<20	<200	52 ± 0.3
4509011301	2021-09-01	1898	<0.5	<200	189 ± 0.4
4509011401	2021-09-21	1476	<35	<200	245 ± 0.5
4509011501	2021-10-03	350	<16	<200	9 ± 0.2
4509011601	2021-10-05	1107	<10	<200	10 ± 0.1
4509011701	2021-10-17	2533	<1	<200	195 ± 0.3
4509011901	2021-11-07	1259	<30	<200	176 ± 0.4
4509012001	2021-11-17	955	<75	<200	10 ± 0.2
4509012101	2021-11-27	1513	<100	<200	6 ± 0.07
4509012201	2021-12-10	1476	<11	<200	249 ± 0.4
4509012301 †	2021-12-23	2411	<1	<306	5 ± 0.06
4509012401	2022-01-05	1474	<15	<300	151 ± 0.3

Neilsen et al. 2004). We set the (tbabs) N_H to the average best-fit line of sight value from Dage et al. (2022) ($2.5 \times 10^{21} \text{ cm}^{-2}$), which is broadly consistent with those found in Neilsen et al. (2004); Pradhan et al. (2020) and Brumback et al. (2023). We freeze this value for all observations, out of concern for degeneracy between the N_H of the tbabs and pcfabs models. We also fit a black-body component (bbody), a cut off power-law (cutoffpl) and three Gaussian components for emission lines, with values adopted from Brumback et al. (2020). The Γ cut-off value is capped at 20 keV for all observations, similar to Brumback et al. (2020) and Dage et al. (2022). Our best-fit model is `tbabs * pcfabs * (bbody + cutoffpl + gauss + gauss + gauss)`.

Except for three pre-eclipse dip observations, the high, intermediate or low states corresponded to the model-predicted count rate, as follows:

- Low, 10 - 50 ct/s
- Intermediate, 50 - 150 ct/s
- High, >150 ct/s

We aim to apply the best fit model described above to all observations, regardless of superorbital state, to investigate changes in obscuration or covering fraction due to changes in the accretion disc during excursion. However, spectra from the low states of the superorbital cycle, when the source flux was decreased, had a lower signal-to-noise (S/N) than the high state data sets. Hence, to apply a consistent spectral model to all data sets while reducing degeneracy in the pcfabs components (see Brumback et al. 2023, for more discussion on model degeneracy), we chose to fix the kT and Γ values in the low and intermediate state spectra to the high state average values, which were 0.19 keV and 0.79, respectively. In this way, we are effectively making the assumption that the underlying continuum has a constant spectral shape. This assumption is valid

when considering the many historic data sets of this source which consistently produce the same spectral shape of a cut-off power-law and soft blackbody component (e.g. the ASCA observations examined in Paul et al. 2002). More recent spectral studies of SMC X-1 with NICER over a period of several months also suggest that the underlying spectral shape remains constant (Brumback et al. 2023). Assuming a constant spectral shape and freezing the low and intermediate state continuum parameters allows us to test whether this assumption holds for the lower signal to noise data.

To further assess the impact of freezing the blackbody kT and Γ values on our pcfabs N_H and covering fraction results, we investigate a representative low state spectrum (ObsID 4509012301). For this fit, we keep the values of kT and Γ fixed, but vary their values by up to 20% from their average values, in increments of 5%. This was done (1) for kT only, while keeping Γ constant, (2) for Γ only, while keeping kT constant, and finally (3) while varying both values simultaneously. In all three cases, variations in the values of kT and Γ did not result in a change in either pcfabs N_H or covering fraction of more than 5%. For this reason, we are confident that holding the shape of the spectral continuum constant in the low state data does not induce artificial errors into the pcfabs values. This is consistent with the results found in (Brumback et al. 2023), where the spectral continuum in SMC X-1 varies little with superorbital period.

The best-fit parameters for this model are in Table 2, and plotted in Figure 2.

3 RESULTS AND DISCUSSION

The first 26 NICER observations in the MOOSE data set span different stages of the system's superorbital period; that is, its high, low, and, intermediate stages. In this analysis we closely monitored the

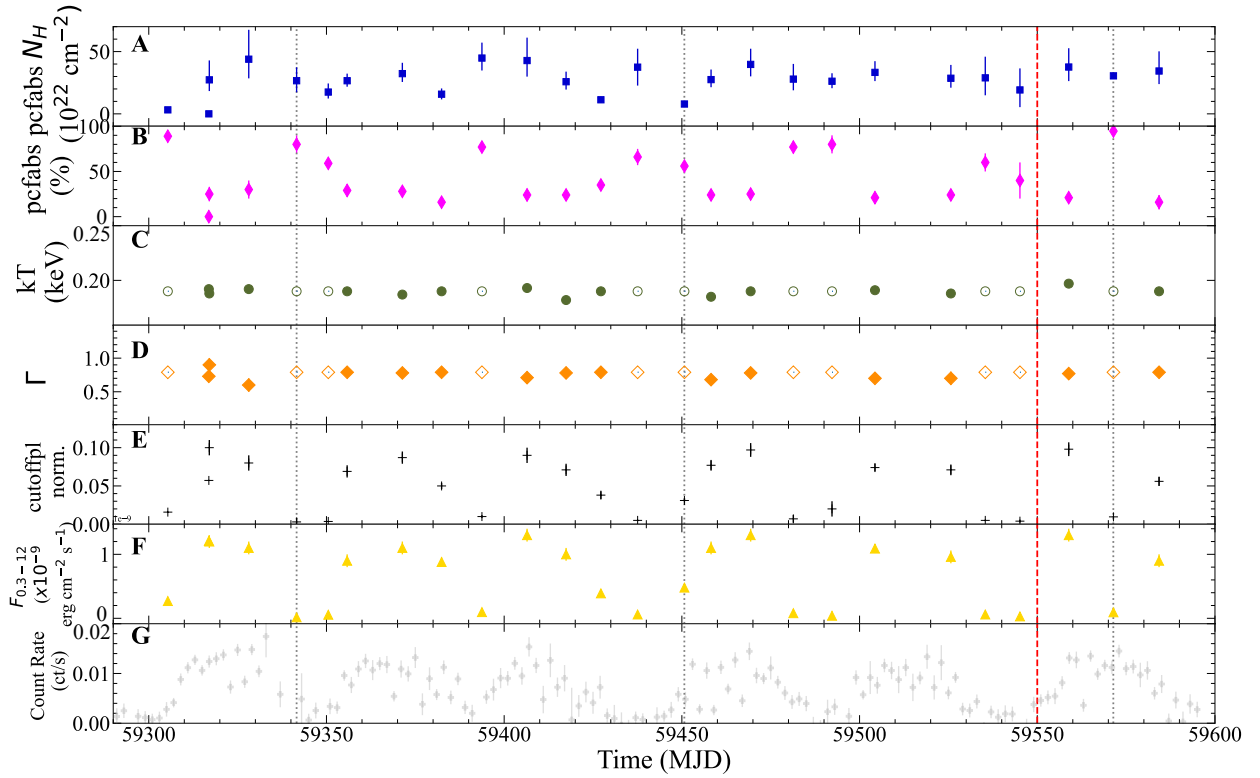


Figure 2. Variation with time (MJD) of the key SMC X-1 X-ray spectral fit parameters: Panel A (blue points) shows $\text{pcfabs } N_H$. Panel B (pink points) shows partial covering fraction. Panel C (green points) shows disc black-body kT . Due to varying spectral quality between high and low state observations, we fix the kT in the low and intermediate state spectra to the average high state value of 0.19. The fixed values are plotted with open symbols, while the free values are plotted with filled symbols. Panel D (orange points) shows the Γ values. As in Panel C, reduced S/N in low state prompted us to fix this value in the low state spectra to the average high state value of 0.79. As before, the fixed points are plotted with open symbols while those where Γ was left variable are plotted with filled symbols. The impact of fixing these kT and Γ values is discussed in §2.2. Panel E (black crosses) shows the normalization of the cut-off power law. Panel F (gold triangles) shows the total flux in the NICER band of 0.3–12 keV. Finally, Panel G (grey points) shows the Swift/BAT light curve during the epoch where these observations were taken. The blackbody kT and Γ values fluctuate very little with superorbital phase, while the $\text{pcfabs } N_H$ and covering fraction both show variations with superorbital period, and in particular the covering fraction shows a mostly smooth variation that is maximized during the superorbital low states. Table 2 details the spectral fit values. In all panels, the red vertical dashed line represents the end of the latest excursion epoch and the grey dotted lines mark the three observations that took place during pre-eclipse dip.

variations in the spectral parameters as a function of superorbital period. Our analysis expands upon previous work by Dage et al. (2022), which examined only the high state spectra during excursion and by Pradhan et al. (2020), which did not consider any data taken during excursion.

In Figure 2, the NICER band flux (Panel E) appears to be directly proportional to the flux of the source (Panel F) and its Swift/BAT count rate (Panel G). Since the power law produces the bulk of our continuum spectral model, it is not surprising that it fluctuates in the same way as the flux of the source.

Figure 2 demonstrates that certain spectral parameters remain relatively unchanged across different superorbital states. Unsurprisingly, the characteristic disc black body temperature (kT) and power-law photon index (Γ) of the continuum exhibit minimal variation. These results support previous findings that the shape of SMC X-1’s high superorbital state X-ray continuum is stable over time (Dage et al. 2022; Brumback et al. 2023). We expand upon these findings by showing that the low and intermediate state spectra are well fit by a similar continuum model, which supports our assumption that the underlying continuum shape does not change. One possible explanation for the apparent stability of SMC X-1’s underlying X-ray continuum is that the inner accretion flow is not sensitive to the rotation of

the disc. Such a scenario would imply that the X-ray spectrum does not change with flux state, it simply modulates in normalization and absorption.

In addition to investigating how SMC X-1’s excursion X-ray spectrum varied across superorbital state, we also investigated the differences between spectra taken during excursion and those taken after. In Figure 2, the red vertical dashed line marks the end of the excursion period, however there is no abrupt change in the variability of the spectral parameters around this epoch.

3.1 Correlation between covering fraction and super-orbital phase

The pcfabs model parameters N_H and covering fraction modulate the shape of the soft end of the X-ray spectrum. Figure 2 shows variability in both of these parameters across the time of our observations, although the N_H appears to become less variable with time.

Our spectral fitting results indicate a strong negative correlation between pcfabs covering fraction and source count rate, thus implying that the partial covering plays a significant role in the shape of the soft spectrum. To investigate the relationship between covering

Table 2. Best fit parameters for our model, $\text{tbabs}^*\text{pcfabs}^*(\text{bbody}+\text{cutoffpl}+\text{gauss}+\text{gauss}+\text{gauss})$, in the 0.3–12 keV band. Observations in the low state (i.e., with a count rate lower than 50 counts/sec) and intermediate state were fit with a model with blackbody temperature and power law index frozen to the best fit values from the high states (see §2.2). The N_{H} for tbabs has been frozen to $2.5 \times 10^{21} \text{cm}^{-2}$. Pre-eclipse dips are marked with †.

ObsID	State	pcfabs N_{H} (10^{22}cm^{-2})	kT (keV)	pcfabs (%)	Γ	Power law norm.	$F_{0.3-12}$ ($\text{erg cm}^{-2} \text{s}^{-1}$)	$\chi^2/\text{d.o.f}$
4509010101	Low	3.2 ± 0.2	0.19	0.89 ± 0.02	0.79	0.0158 ± 0.0007	$(2.7 \pm 0.1) \times 10^{-10}$	176/130
4509010102	High	< 0.02	0.192 ± 0.002	0.00 ± 0.05	$0.73^{+0.03}_{-0.05}$	0.0572 ± 0.0008	$(1.21 \pm 0.02) \times 10^{-9}$	300/161
4509010103	High	$27.3^{+15.6}_{-9.0}$	0.191 ± 0.003	0.24 ± 0.08	0.9 ± 0.1	0.10 ± 0.01	$(1.2 \pm 0.1) \times 10^{-9}$	159/147
4509010301	High	$43.9^{+23.6}_{-15.4}$	0.192 ± 0.004	0.3 ± 0.1	0.6 ± 0.1	0.08 ± 0.01	$(1.1 \pm 0.1) \times 10^{-9}$	143/143
4509010401 †	Low	$26.6^{+10.8}_{-9.3}$	0.19	0.8 ± 0.1	0.79	$0.003^{+0.005}_{-0.001}$	$(1.6 \pm 0.2) \times 10^{-11}$	139/111
4509010501	Low	$17.5^{+6.9}_{-5.2}$	0.19	0.59 ± 0.05	0.79	0.0036 ± 0.0006	$(5.6 \pm 0.9) \times 10^{-11}$	240/124
4509010601	Intermediate	$26.6^{+5.7}_{-4.8}$	0.19	0.29 ± 0.07	0.79	0.069 ± 0.008	$(9 \pm 1) \times 10^{-10}$	177/130
4509010701	High	$32.3^{+8.7}_{-6.7}$	0.187 ± 0.002	0.28 ± 0.05	0.78 ± 0.04	0.087 ± 0.008	$(1.1 \pm 0.1) \times 10^{-9}$	268/162
4509010801	Intermediate	$15.8^{+4.6}_{-4.2}$	0.19	0.16 ± 0.05	0.79	0.050 ± 0.004	$(8.8 \pm 0.7) \times 10^{-10}$	226/160
4509010802	Low	$44.8^{+12.4}_{-10.0}$	0.19	0.77 ± 0.05	0.79	0.010 ± 0.002	$(1.0 \pm 0.2) \times 10^{-9}$	244/126
4509010803	High	$42.8^{+18.4}_{-12.9}$	0.193 ± 0.002	0.24 ± 0.07	0.71 ± 0.09	0.09 ± 0.01	$(1.3 \pm 0.1) \times 10^{-9}$	187/159
4509010901	High	$25.8^{+8.1}_{-6.3}$	0.182 ± 0.003	0.24 ± 0.06	0.78 ± 0.09	0.071 ± 0.008	$(1.0 \pm 0.1) \times 10^{-9}$	171/156
4509011001	Intermediate	11.3 ± 2.5	0.19	0.35 ± 0.06	0.79	0.038 ± 0.005	$(3.9 \pm 0.5) \times 10^{-10}$	189/130
4509011101	Low	37.5 ± 14.8	0.19	0.66 ± 0.00	0.79	0.005 ± 0.001	$(6 \pm 1) \times 10^{-11}$	324/125
4509011201 †	Low	7.9 ± 1.2	0.19	0.56 ± 0.02	0.79	0.031 ± 0.003	$(4.8 \pm 0.5) \times 10^{-10}$	334/130
4509011301	High	$27.5^{+8.1}_{-6.1}$	0.185 ± 0.002	0.24 ± 0.05	0.68 ± 0.08	0.077 ± 0.007	$(1.1 \pm 0.1) \times 10^{-9}$	177/160
4509011401	High	$39.7^{+12.7}_{-9.6}$	0.190 ± 0.002	0.25 ± 0.06	0.78 ± 0.07	0.097 ± 0.009	$(1.3 \pm 0.1) \times 10^{-9}$	254/161
4509011501	Low	$27.9^{+12.2}_{-9.0}$	0.19	0.77 ± 0.07	0.79	0.007 ± 0.005	$(8 \pm 2) \times 10^{-11}$	137/117
4509011601	Low	$26.2^{+6.4}_{-5.6}$	0.19	0.8 ± 0.1	0.79	0.02 ± 0.01	$(4 \pm 3) \times 10^{-11}$	435/130
4509011701	High	$33.3^{+9.0}_{-7.0}$	0.191 ± 0.002	0.21 ± 0.05	0.70 ± 0.06	0.074 ± 0.005	$(1.09 \pm 0.07) \times 10^{-9}$	267/160
4509011901	High	$28.6^{+10.7}_{-7.6}$	0.188 ± 0.003	0.24 ± 0.06	0.7 ± 0.1	0.071 ± 0.007	$(1.0 \pm 0.1) \times 10^{-9}$	170/154
4509012001	Low	$28.9^{+17.0}_{-14.0}$	0.19	0.6 ± 0.1	0.79	0.005 ± 0.001	$(6 \pm 1) \times 10^{-11}$	282/123
4509012101	Low	$19.2^{+17.3}_{-13.8}$	0.19	0.4 ± 0.2	0.79	0.004 ± 0.002	$(3 \pm 2) \times 10^{-11}$	221/126
4509012201	High	$37.6^{+15.1}_{-11.3}$	0.197 ± 0.002	0.21 ± 0.06	0.77 ± 0.08	0.098 ± 0.009	$(1.3 \pm 0.1) \times 10^{-9}$	223/159
4509012301 †	Low	30.4 ± 1.9	0.19	0.947 ± 0.004	0.79	0.0096 ± 0.0008	$(9.4 \pm 0.8) \times 10^{-11}$	441/130
4509012401	Intermediate	$34.4^{+15.8}_{-10.5}$	0.19	0.16 ± 0.08	0.79	0.056 ± 0.006	$(9 \pm 1) \times 10^{-10}$	193/130

fraction and super-orbital state, we plotted the covering fraction as a function of the NICER count rate in Figure 3. We found that the covering fraction and super-orbital state are inversely related, with the high-state observations having the largest count rates and smallest covering fractions and the low states having the smallest count rates and highest covering fractions. This relationship fits with our understanding of the warped accretion disc precession that drives the super-orbital period. To investigate the relationship between these two spectral parameters and source count rate in detail, we calculated the Pearson linear correlation coefficient for N_{H} against count rate and for pcfabs against count rate, which provides additional insights.

For the relationship between N_{H} and count rate, we obtained a correlation coefficient of 0.24 with a null hypothesis probability of

0.23, indicating no significant correlation. To determine the influence of outliers, we performed 10^4 bootstrap simulations. The resulting correlation coefficient distribution revealed a peak at $r = 0.25$ with a standard deviation of 0.19, suggesting a large overlap with the null hypothesis. Additionally, we carried out 10^4 Monte Carlo simulations to test the impact of parameter uncertainties on the correlation coefficient. By considering the N_{H} uncertainty as the standard deviation in a Gaussian distribution for each simulation, we derived a correlation coefficient of -0.02 ± 0.2 . This indicates that the correlation between N_{H} and the count rate is statistically negligible.

On the other hand, when examining the anti-correlation between pcfabs and count rate, we found a more substantial negative correlation with a coefficient of -0.86 , with a null hypothesis probability of 2.3×10^{-8} . This implies a consistent inverse relationship between

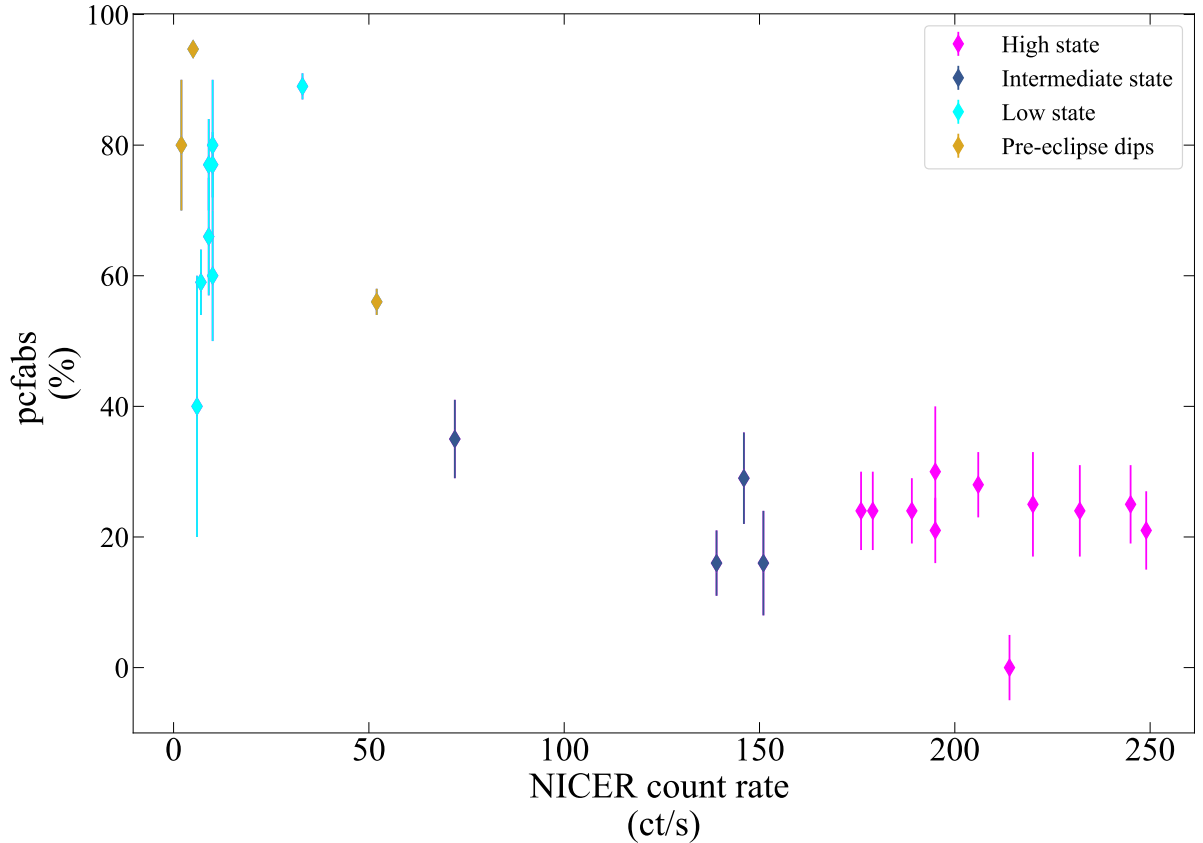


Figure 3. Best fit partial covering fraction versus NICER count rate. The gold points denote pre-eclipse dips, the cyan points are low state observations, the dark blue are intermediate state, and the fuchsia are high state. Overall, the trend between partial covering fraction and superorbital period state appear to be correlated, indicating that the source’s low states coincide with a higher percentage of covering, and vice versa. As seen in Table 1, the observation lengths vary significantly, leading to larger error bars in shorter observations.

pcfabs and count rate. Employing the bootstrap method resulted in a single-peaked distribution of the correlation coefficient, with an average value of -0.86 and a standard deviation of 0.04 . Similarly, Monte Carlo simulations produced a correlation coefficient of -0.83 ± 0.04 , consistent with the bootstrap findings. Thus, the observed anticorrelation between pcfabs and the count rate is highly significant compared to any relation between N_{H} and the count rate.

Under a model in which absorption by a warped, precessing disc is responsible for the superorbital modulation, we expect maximum obscuration during the super-orbital low states and minimum obscuration during the super-orbital high states. The only places where we see deviation from the inverse relationship between partial covering fraction and super-orbital period are during pre-eclipse dips (see grey dotted lines in Fig. 2). These dips are orbital in nature and therefore can occur during the orbital high state. Our dataset captured 3 pre-eclipse dips, defined as having an orbital phase higher than 0.8, based on the ephemeris from Falanga et al. (2015). These three observations, ObsIDs 4509010401, 4509011201, 4509012301 all showed high covering fractions, which agrees with the interpretation of similar features in Her X-1 (e.g., Giacconi et al. 1973) as increased obscuration by the “splash zone” where the accretion stream impacts the disc.

Additionally, Brumback et al. (2023) analysed 18 NICER observations of SMC X-1 during four different super-orbital high states and found that the continuum parameters (blackbody temperature kT and Γ) showed very little change between super-orbital high states. In-

stead, they found that the most significant changes in spectral shape occurred between spectra from the superorbital intermediate state (when the source is increasing in luminosity as the accretion disc moves out of the line of sight) and the high state. Brumback et al. (2023) suggested that the underlying spectral continuum shape is constant, but is sensitive to changes in obscuration caused by the rotation angle of the disc. Our results from this analysis, particularly the inverse relationship between the covering fraction and superorbital period state, support these results and the conclusion that the inner accretion flow in SMC X-1 is insensitive to changes in the outer disc shape, although we are assuming that the underlying model continuum does not change significantly in the high/low state.

While our assumption of a constant spectral state seems well supported by the data, the full picture may be more complex. Pradhan et al. (2020) jointly fit SUZAKU and NuSTAR spectra and found that the power-law normalization (in the hard energy band of both detectors) is variable. From their spectroscopic fits, they conclude that there is evidence for a change in the partial covering fraction of the inner disc region, correlated with the superorbital variation. However, due to the power-law variability in the hard X-ray band, they suggest that there is another mechanism behind the superorbital variation, i.e., a change in the instantaneous accretion rate. We cannot make a direct comparison to the Pradhan et al. (2020) spectra as our NICER observations do not extend above 12 keV, and do not fully constrain the power-law cut-off (as noted in Dage et al. 2022, the cut-off extends beyond the range to which NICER is sensitive).

Like Pradhan et al. (2020), a correlation between the power-law normalization component (K of `xspec`'s `cutoffpl`) and the 0.3–12.0 keV model flux is apparent in the excursion data (panels E and F of Figure 2), as expected for any major component of the source emission. However, our fits strongly suggest that the only correlation between the superorbital period and the X-ray spectral shape in the soft band is due to variation in the partial covering fraction of the inner accretion disc.

4 CONCLUSIONS AND FUTURE WORK

We performed X-ray spectroscopy of 26 NICER observations of the neutron star pulsar SMC X-1 to investigate changes in spectral shape across superorbital states within excursion for the first time, and compare to data from outside excursion. Our best fit model for these observations is a black-body and cut-off power-law continuum with several emission lines that is absorbed by a neutral absorber and a partial covering fraction, and we assume that the underlying model continuum does not change significantly in the low state. Our findings are summarized as follows:

- The same spectral model can adequately describe all of the data regardless of super-orbital state or excursion status.
- The partial covering parameter is inversely related to source count rate (a proxy for super-orbital state). Pradhan et al. (2020) observed this relationship for non-excursion data, and the trend carries on in excursion. This implies a warped accretion disc is obscuring the source, and the super-orbital period is caused by the rotating warped accretion disc covering flux from the neutron star.
- The spectral parameters show no change in the immediate vicinity of the end of excursion. N_{H} potentially shows a transition from an epoch of higher variability to a more stable epoch approximately 70 days before the end of excursion, but the correlation between these behaviors is unclear.

The next step will be to study the later observations in the MOOSE data set, which continue after the end of excursion and could provide more insights into the difference in spectral shape and parameter variability between excursion and non-excursion data.

The presence of soft emission lines in our data is also interesting. These disc-formed emission lines are effective observational tracers of how material in the accretion disc behaves and evolves over time. Throughout a binary orbit, line profile shape/strength will change, carrying within it an imprint of the evolving source of X-rays heating the accretion disc itself. An empirical connection between the line emitting regions, and physical properties of the X-ray source heating the disc, has proved to be an effective observational tool for understanding the structure and geometry of the gas making up accretion discs in LMXBs see (Tetarenko et al. 2020, 2023). In the future, a similar technique used for LMXBs could realistically be adapted and applied to SMC X-1, using a suitable model for X-ray irradiation in X-ray pulsar sources (e.g., Hickox & Vrtilek 2005).

ACKNOWLEDGEMENTS

The authors thank the NICER team for flexible scheduling of the observations, and Alex Tetarenko for helpful discussions. RK acknowledges the Trottier Space Institute at McGill summer undergraduate fellowship program for supporting this project. KCD and DH acknowledge funding from the Natural Sciences and Engineering Research Council of Canada (NSERC) and the Canada Research

Chairs (CRC) program. KCD acknowledges fellowship funding from Fonds de Recherche du Québec – Nature et Technologies, Bourses de recherche postdoctorale B3X no. 319864 and support provided by NASA through the NASA Hubble Fellowship grant HST-HF2-51528 awarded by the Space Telescope Science Institute, which is operated by the Association of Universities for Research in Astronomy, Inc., for NASA, under contract NAS5–26555. MCB acknowledges support from NASA Grant 80NSSC23K0619. CPH acknowledges support from the National Science and Technology Council in Taiwan through grant 112-2112-M-018-004-MY3. BET acknowledges support from the Trottier Space Institute (TSI) at McGill, through an TSI Fellowship.

This research has made use of data and/or software provided by the High Energy Astrophysics Science Archive Research Center (HEASARC), which is a service of the Astrophysics Science Division at NASA/GSFC.

DATA AVAILABILITY

The NICER observations are publicly available through HEASARC (<https://heasarc.gsfc.nasa.gov/docs/archive.html>).

REFERENCES

- Arnaud K. A., 1996, in Jacoby G. H., Barnes J., eds, *Astronomical Society of the Pacific Conference Series Vol. 101, Astronomical Data Analysis Software and Systems V*. p. 17
- Bachetti M., et al., 2020, *ApJ*, **891**, 44
- Brumback M. C., Hickox R. C., Fürst F. S., Pottschmidt K., Tomsick J. A., Wilms J., 2020, *ApJ*, **888**, 125
- Brumback M. C., et al., 2022, *ApJ*, **926**, 187
- Brumback M. C., Vasilopoulos G., Coley J. B., Dage K., Miller J. M., 2023, *arXiv e-prints*, p. [arXiv:2307.15591](https://arxiv.org/abs/2307.15591)
- Clarkson W. I., Charles P. A., Coe M. J., Laycock S., 2003, *MNRAS*, **343**, 1213
- Dage K. C., Clarkson W. I., Charles P. A., Laycock S. G. T., Shih I. C., 2019, *MNRAS*, **482**, 337
- Dage K. C., et al., 2022, *MNRAS*, **514**, 5457
- Falanga M., Bozzo E., Lutovinov A., Bonnet-Bidaud J. M., Fetisova Y., Puls J., 2015, *A&A*, **577**, A130
- Foulkes S. B., Haswell C. A., Murray J. R., 2006, *MNRAS*, **366**, 1399
- Gendreau K. C., et al., 2016, in den Herder J.-W. A., Takahashi T., Bautz M., eds, *Society of Photo-Optical Instrumentation Engineers (SPIE) Conference Series Vol. 9905, Space Telescopes and Instrumentation 2016: Ultraviolet to Gamma Ray*. p. 99051H, doi:10.1117/12.2231304
- Giacconi R., Gursky H., Kellogg E., Levinson R., Schreier E., Tananbaum H., 1973, *ApJ*, **184**, 227
- Gruber D. E., Rothschild R. E., 1984, *ApJ*, **283**, 546
- Hickox R. C., Vrtilek S. D., 2005, *ApJ*, **633**, 1064
- Hickox R. C., Narayan R., Kallman T. R., 2004, *ApJ*, **614**, 881
- Hu C.-P., Chou Y., Yang T.-C., Su Y.-H., 2013a, *ApJ*, **773**, 58
- Hu C.-P., Chou Y., Yang T.-C., Su Y.-H., 2013b, *ApJ*, **773**, 58
- Hu C.-P., Mihara T., Sugizaki M., Ueda Y., Enoto T., 2019, *ApJ*, **885**, 123
- Hu C.-P., et al., 2023, *MNRAS*,
- Kaastra J. S., Bleeker J. A. M., 2016, *A&A*, **587**, A151
- Lucke R., Yentis D., Friedman H., Fritz G., Shulman S., 1976, *ApJ*, **206**, L25
- Naik S., Paul B., 2004, *A&A*, **418**, 655
- Neilsen J., Hickox R. C., Vrtilek S. D., 2004, *ApJ*, **616**, L135
- Ogilvie G. I., Dubus G., 2001, *MNRAS*, **320**, 485
- Paul B., Nagase F., Endo T., Dotani T., Yokogawa J., Nishiuchi M., 2002, *ApJ*, **579**, 411
- Pike S. N., et al., 2019, *ApJ*, **875**, 144
- Pradhan P., Maitra C., Paul B., 2020, *ApJ*, **895**, 10
- Raichur H., Paul B., 2010, *MNRAS*, **401**, 1532

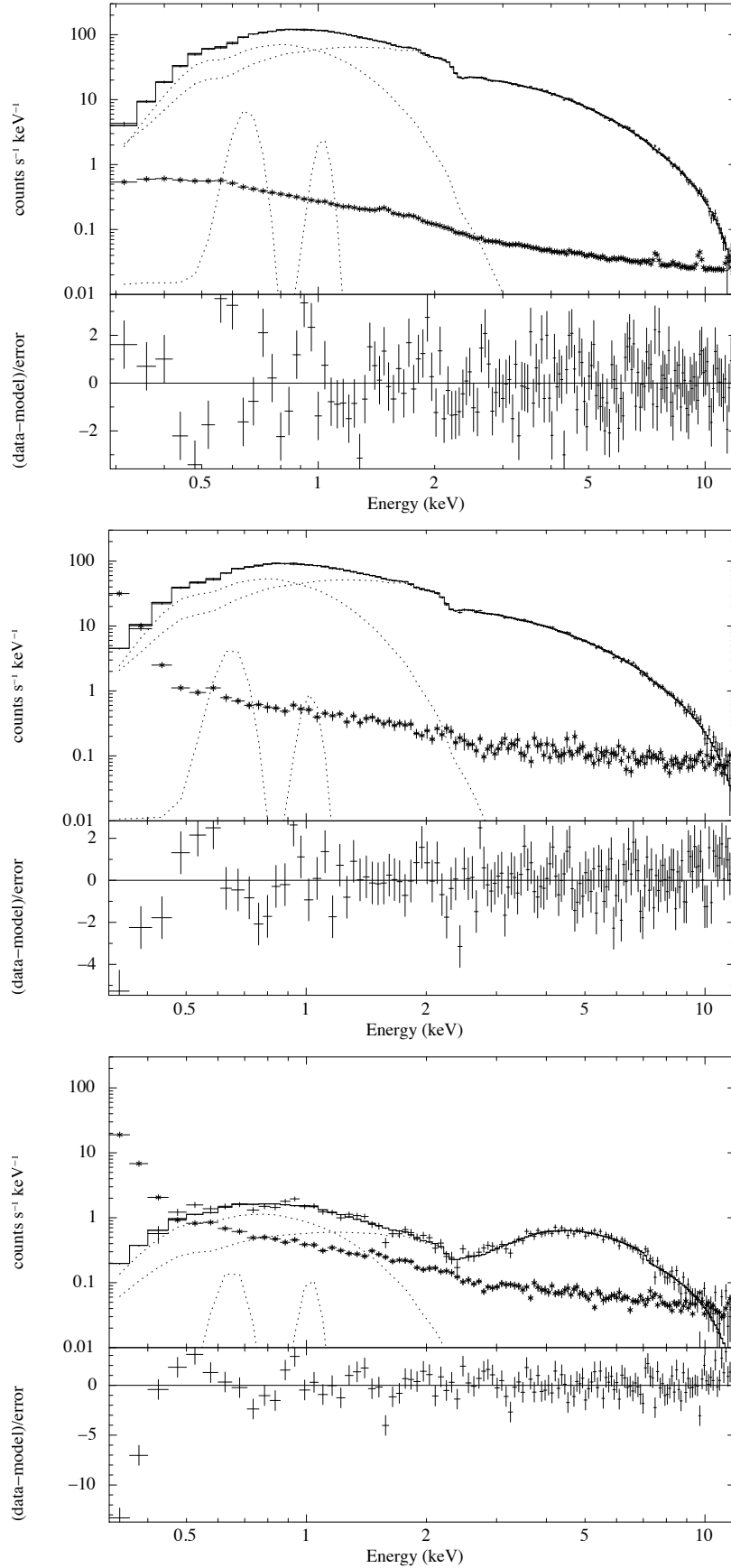


Figure 4. Representative high state (top panel, ObsID 4509011701), intermediate state (middle panel, ObsID 4509012401), and low state (bottom panel, ObsID 4509012301) spectra fit with our best fit model.

- Remillard R. A., et al., 2022, *AJ*, 163, 130
- Tetarenko B. E., Dubus G., Marcel G., Done C., Clavel M., 2020, *MNRAS*, 495, 3666
- Tetarenko B. E., Shaw A. W., Charles P. A., 2023, *MNRAS*, 526, 6284
- Thomas J. K., Charles P. A., Buckley D. A. H., Kotze M. M., Lasota J.-P., Potter S. B., Steiner J. F., Paice J. A., 2022, *MNRAS*, 509, 1062
- Townsend L. J., Charles P. A., 2020, *MNRAS*, 495
- Verner D. A., Ferland G. J., Korista K. T., Yakovlev D. G., 1996, *ApJ*, 465, 487
- Wilms J., Allen A., McCray R., 2000, *ApJ*, 542, 914
- Wojdowski P., Clark G. W., Levine A. M., Woo J. W., Zhang S. N., 1998, *ApJ*, 502, 253
- Woo J. W., Clark G. W., Blondin J. M., Kallman T. R., Nagase F., 1995, *ApJ*, 445, 896

This paper has been typeset from a $\text{\TeX}/\text{\LaTeX}$ file prepared by the author.